

Outflows, inflows, and young stars in the inner 200 pc of the Seyfert galaxy NGC 2110

Marlon R. Diniz¹,¹★ Rogemar A. Riffel^{1,2},^{1,2} Thaisa Storchi-Bergmann³
and Rogério Riffel^{1,3}

¹*Departamento de Física, Centro de Ciências Naturais e Exatas, Universidade Federal de Santa Maria, Santa Maria, RS, 97105-900, Brazil*

²*Department of Physics & Astronomy, Johns Hopkins University, Bloomberg Center, 3400 N. Charles St, Baltimore, MD 21218, USA*

³*Instituto de Física, Universidade Federal do Rio Grande do Sul, CP 15051, Porto Alegre, RS, 91501-970, Brazil*

Accepted 2019 May 10. Received 2019 May 9; in original form 2019 March 14

ABSTRACT

We present a 2D mapping of stellar population age components, emission-line fluxes, gas excitation, and kinematics within the inner ~ 200 pc of the Seyfert 2 galaxy NGC 2110. We used the Gemini North Integral Field Spectrograph (NIFS) in the J and K bands at a spatial resolution of ~ 22 pc. The unresolved nuclear continuum is originated in combined contributions of young stellar population (SP; age ≤ 100 Myr), a featureless AGN continuum and hot dust emission. The young-intermediate SP ($100 < \text{age} \leq 700$ Myr) is distributed in a ring-shaped structure at ≈ 140 pc from the nucleus, which is roughly coincident with the lowest values of the stellar velocity dispersion. In the inner ≈ 115 pc the old SP (age > 2 Gyr) is dominant. The [Fe II] $\lambda 1.2570$ μm emission-line flux distribution is correlated with the radio emission and its kinematics comprise two components, one from gas rotating in the galaxy plane and another from gas in outflow within a bicone-oriented along north–south. These outflows seem to originate in the interaction of the radio jet with the ambient gas producing shocks that are the main excitation mechanism of the [Fe II] emission. We estimate: (1) an ionized gas mass outflow rate of $\sim 0.5 M_{\odot} \text{ yr}^{-1}$ at ~ 70 pc from the nucleus; and (2) a kinetic power for the outflow of only 0.05 per cent of the AGN bolometric luminosity implying weak feedback effect on the galaxy.

Key words: galaxies: individual (NGC 2110) – galaxies: kinematics and dynamics – galaxies: Seyfert – infrared: galaxies.

1 INTRODUCTION

Detailed studies on the gas kinematics and excitation in the inner region (< 1 kpc) of active galaxies are necessary to better understand feeding and feedback processes of Active Galactic Nuclei (AGNs) and their effect on galaxy evolution. In addition, the mapping of the stellar populations age distributions in the vicinity of AGN is fundamental to investigate a possible relation between AGN activity and star formation.

In recent years, theoretical and observational studies have been carried out to investigate how the gas is transferred from galactic to nuclear scales (e.g. Knapen, Shlosman & Peletier 2000; Emsellem et al. 2001; Maciejewski et al. 2002; Crenshaw, Kraemer & Gabel 2003; Fathi et al. 2005; Riffel et al. 2008; Davies et al. 2009; Schartmann et al. 2010; Hopkins et al. 2012; Schartmann et al. 2014). For a recent review on observational constraints on the

feeding of supermassive black holes, see Storchi-Bergmann & Schnorr-Müller (2019). Gas inflows can either trigger star formation in the circumnuclear region of the galaxy and/or initiate an episode of nuclear activity. In fact, circumnuclear star-forming regions are often observed in active galaxies (e.g. Morgan 1958; Sersic & Pastoriza 1967; Imanishi & Dudley 2000; Rodríguez-Ardila & Viegas 2003; Riffel et al. 2007, 2009b, 2016; Hennig et al. 2018).

For luminous AGN ($L_{\text{bol}} \gtrsim 10^{43} \text{ erg s}^{-1}$), the feedback processes – e.g. effect of the radiation and winds emitted from accretion disc on the host galaxy – are claimed to play an important role in the evolution of galaxies (Bower et al. 2006; Somerville et al. 2008). However, for lower luminosity objects, the effect of the AGN in the host galaxy is still an open question. Comparing the gas kinematics to the stellar kinematics, on scales from tens to hundreds pc, allows the mapping of AGN winds and their effect on the host galaxy properties.

One way to verify how this interaction occurs is through the study of the excitation and kinematics of the gas in the Narrow Line Region (NLR). Using the emission lines in the near-infrared (NIR),

* E-mail: diniz.mr@gmail.com

such as [Fe II] $\lambda\lambda$ 1.257, 1.644 μm , Pa β , Br γ , and H $_2$ λ 2.1218 μm , one can map the main mechanisms of gas excitation as well as the kinematics of different gas phases. While some works point out a correlation between the [Fe II] and the radio emission, indicating that the [Fe II] emission in AGNs is originated by shocks due to radio jets (Forbes & Ward 1993; Blietz et al. 1994), others argue that its emission is due to photoionization by the nuclear source (Simpson et al. 1996; Das et al. 2005, 2006).

The mapping and characterization of the stellar populations (SPs) in active galaxies is needed in order to investigate the relation between nuclear activity and star formation, providing ingredients – such as star formation history (SFH) and star formation rate (SFR) – to constrain galaxy evolution models.

An advantage of using the NIR instead of optical observations is that the former allows the study of more obscured regions. This is due to the fact that the extinction is smaller in the NIR than in optical bands, although the detection of spectral features of young stars in this spectral range is not an easy task (Maraston 2005; Riffel et al. 2007, 2008; Martins et al. 2013; Zibetti et al. 2013; Riffel et al. 2015; Hennig et al. 2018).

By performing stellar population synthesis using models of evolutionary population synthesis (EPS), which include a suitable treatment of stars in the Thermally Pulsing Asymptotic Giant Branch (TP-AGB) phase (Maraston 2005), it is possible to study in detail the properties of the stellar populations that dominate the NIR emission. This is due to the fact that these models include the contributions of molecules such as CN and TiO, characteristic of stars in this evolutionary phase.

Our group AGNIFS (for AGN Integral Field Spectroscopy), uses NIR data obtained with the Gemini NIFS instrument at the Gemini North Telescope. We have been finding, as a frequent characteristic of the circumnuclear SP of AGN host galaxies, an important contribution of an intermediate age (~ 700 Myr) component (Riffel et al. 2010b, 2011; Storchi-Bergmann et al. 2012; Schönell et al. 2017; Diniz et al. 2017; Dahmer-Hahn et al. 2019; Dametto et al. 2019).

In this work, we use NIFS observations to map the gas excitation and kinematics, as well as the stellar populations, of the inner 200 pc radius of NGC 2110, an SO galaxy hosting an Sy 2 nucleus and located at a distance of 30.2 Mpc (from NED,¹ derived assuming a redshift of 0.007789 and $H_0 = 73 \text{ km s}^{-1} \text{ Mpc}^{-1}$), for which 1'' corresponds to 146 pc. In a previous study (Diniz et al. 2015), we used observations in the K band to map the molecular and ionized gas kinematics. The flux distributions of H $_2$ and Br γ emission lines were found to be distinct: while the H $_2$ emission is observed over the whole field of view ($3'' \times 3''$), the Br γ emission is collimated along PA $\approx -30^\circ$. The gas kinematics revealed inflows towards the nucleus along spiral arms as well as a compact outflow within the inner ≈ 70 pc. The derived mass inflow rate and outflow rates in warm molecular gas (that originates the K-band H $_2$ emission) are $\approx 5 \times 10^{-4} \text{ M}_\odot \text{ yr}^{-1}$ and $\approx 4 \times 10^{-4} \text{ M}_\odot \text{ yr}^{-1}$, respectively. We concluded that the main H $_2$ excitation mechanism is heating of the gas by X-rays emitted from the AGN.

Durré & Mould (2014) have also recently presented NIR IFS of the central region of NGC 2110 using J-band data obtained with the Keck I OSIRIS instrument and reported the detection of star clusters along with a 90×35 pc bar of shocked gas around the nucleus of NGC 2110. They derived a star formation rate of $0.3 \text{ M}_\odot \text{ yr}^{-1}$ and argue that the star formation is triggered by the AGN feedback.

Optical IFS of the inner $1.1 \times 1.6 \text{ kpc}^2$ ($7'' \times 10''$) obtained with the Gemini GMOS instrument by Schnorr-Müller et al. (2014), revealed four kinematic components: (i) a cold gas disc (with velocity dispersion (σ) in the range $60\text{--}90 \text{ km s}^{-1}$) consistent with the H $_2$ kinematics of Diniz et al. (2015), (ii) a warm gas disc ($\sigma = 100\text{--}220 \text{ km s}^{-1}$), (iii) a nuclear outflow ($\sigma = 220\text{--}600 \text{ km s}^{-1}$) and (iv) a cloud ($\sigma = 60\text{--}80 \text{ km s}^{-1}$), which was identified as ‘the northern cloud’. In agreement with Diniz et al. (2015), these authors identified both inflowing and outflowing gas. They derived an ionized gas mass inflow and outflow rates of $\approx 2 \times 10^{-2} \text{ M}_\odot \text{ yr}^{-1}$ and $\approx 0.9 \text{ M}_\odot \text{ yr}^{-1}$, respectively.

This paper is organized as follows: in Section 2, we describe the observations and data reduction procedures, Section 3 presents 2D maps for the emission-line fluxes, gas kinematics, flux ratios, and contributions of the stellar populations to the observed continuum emission. The results are discussed in Section 4 and Section 5 summarizes the conclusions of this work.

2 OBSERVATIONS, DATA REDUCTION, AND ANALYSIS

Two-dimensional (2D) NIR spectroscopic data were obtained at the Gemini North Telescope with the Near-Infrared Integral Field Spectrograph (NIFS; McGregor et al. 2003), under the programmes GN-2010B-Q-25 and GN-2015B-Q-29. NGC 2110 is part of the sample of the Brazilian Gemini Large Program ‘NIFS survey of feeding and feedback processes in nearby active galaxies’ (P.I. Storchi-Bergmann) described in Riffel et al. (2018) and aimed to obtain J and K bands IFS of a sample of 20 nearby AGNs. NIFS has a square field of view of $3'' \times 3''$, which corresponds to $\sim 440 \times 440 \text{ pc}^2$ at NGC 2110.

The data reduction was accomplished using tasks contained in the NIFS package, which are part of GEMINI IRAF package, as well as standard IRAF tasks and Interactive Data Language (IDL) routines. The process followed the standard procedure of NIR spectroscopic data reduction described in previous works (e.g. Riffel et al. 2008; Diniz et al. 2015; Riffel et al. 2017). The K band data cube was already used in Diniz et al. (2015) and Riffel et al. (2017) to study the molecular gas and stellar kinematics. The final data cubes were created with a spatial sampling (spaxel) of $0''.05 \times 0''.05$.

We have used the long-slit nuclear spectrum of NGC 2110 presented by Riffel, Rodríguez-Ardila & Pastoriza (2006) to cross-calibrate the J and K bands in the NIFS data. The long-slit spectrum was obtained with the instrument SpeX of the NASA 3 m Infrared Telescope Facility (IRTF) within an aperture of $0''.8 \times 1''.6$ with the slit oriented along PA = 20° using the short cross-dispersed mode that covers the spectral range from 0.8 to 2.4 μm . We have extracted the J and K NIFS spectra within the same aperture of the SpeX spectrum, and then scaled them to the same fluxes. In Fig. 1, we present the comparison of the final NIFS nuclear spectrum with that of Riffel, Rodríguez-Ardila & Pastoriza (2006). Both the continuum and emission-line fluxes are consistent between NIFS and SpeX data.

The spatial resolution, as obtained from the full width at half-maximum (FWHM) of the brightness profile of the telluric standard star, is $0''.13$ and $0''.15$ for the J and K band, respectively. The spectral resolution is $\sim 46 \text{ km s}^{-1}$ for both J and K bands, as obtained from the typical FWHM of the arc lamp lines.

2.1 Spectral synthesis

The integrated spectrum of an active galaxy consists of several components, such as stellar, gas and dust emission, as well as the

¹NASA/IPAC extragalactic database

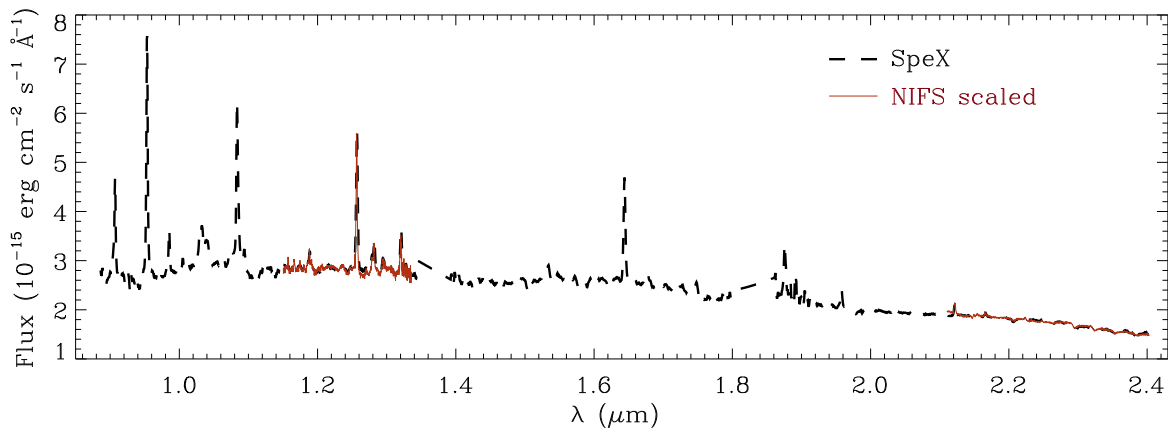


Figure 1. Comparison of the NIFS (red continuum line) nuclear spectrum after calibration of the data cubes using the IRTF SpeX spectrum of Riffel, Rodríguez-Ardila & Pastoriza (2006). Both spectra were obtained with an aperture of $0''.8 \times 1''.6$ oriented along $PA = 20^\circ$.

AGN torus and accretion disc components. The synthesis process combines a set of spectra of Simple Stellar Populations (SSPs) as well as models for the AGN components, as part of the base of elements used to reproduce the galaxy spectrum. The process allows to retrieve information on the per cent contribution of components of different ages and metallicities, as well as of the AGN components.

We performed spectral synthesis using the STARLIGHT code (Cid Fernandes et al. 2004, 2005a,b; Asari et al. 2007) in order to quantify the contribution of each component to the spectrum of each spaxel. The code fits the continuum and absorption features of the spectrum by a combination in different proportions of each SSP and AGN components in the base.

We have used the SSP models of Maraston (2005), which are described in Riffel et al. (2009), because they include empirical data with contribution from stars in the TP-AGB phase. This is important because the NIR range presents certain molecular absorption features, such as CN, CO, VO, ZrO and TiO, which are attributed to evolved stars belonging to the Red Giant Branch (RGB) and these TP-AGB stars (e.g. Riffel et al. 2015).

The SSPs comprise 12 age components ($t = 0.01, 0.03, 0.05, 0.1, 0.2, 0.5, 0.7, 1, 2, 5, 9, 13$ Gyr) and 4 metallicities ($Z = 0.02, 0.5, 1, 2 Z_\odot$), together with black-body (BB) functions for temperatures in the range 700–1400 K in steps of 100 K and a power-law ($F_\nu \propto \nu^{-1.5}$), in order to account, respectively, for possible contributions from hot dust emission (the AGN torus) and from the AGN.

In short, the STARLIGHT code uses a combination of numeric methods to determine the stellar mass, extinction (A_V), ages, metallicities, radial velocity, and stellar velocity dispersion. For each observed spectrum, the synthesis process generates a list of parameters and a synthetic spectrum. The J- and K-band data cubes were combined using the peak of the continuum emission as reference, and in order to increase the signal-to-noise ratio of the spectra, we have rebinned the combined datacube to $0''.15 \times 0''.15$ spaxels before performing the spectral synthesis.

2.2 Emission-line fitting

In order to map the emission-line flux distributions, centroid velocities, and velocity dispersion, we have fitted the line profiles with Gaussian curves. The corresponding maps for the K-band emission lines were already presented in Diniz et al. (2015); here, we focus on the J-band. The J-band spectra of NGC 2110 present

strong emission of [P II] at $1.1886 \mu\text{m}$, [Fe II] at $1.2570 \mu\text{m}$, and $\text{Pa}\beta$ at $1.2822 \mu\text{m}$. We have used the PROFIT routine (Riffel 2010a) to fit the emission-line profiles. This routine uses the MPFITFUN routine (Markwardt et al. 2009) to perform a non-linear least-squares fit and outputs measurements for the flux, centroid velocity, and velocity dispersion of each fitted emission-line at each spaxel, as well as their corresponding uncertainties. We do not subtract the stellar population contribution before the fitting of the emission-line profiles, as the SSP models available in the NIR spectral range have much lower spectral resolution than the NIFS data. Indeed, the expected effect on the emission-line fluxes is within the uncertainties (Martins et al. 2013; Dametto et al. 2014). The continuum underneath each line is fitted by a first-order polynomial, as each emission-line is fitted separately and only a small spectral range is included in the fit.

In Fig. 2, we show examples of the J-band spectra extracted within circular apertures with radius $0''.25$, centred at the locations of the spectra shown in fig. 1 of Diniz et al. (2015). The first spectrum corresponds to the nucleus, the second to a typical extra-nuclear position, the third to a region of enhanced H_2 emission, and the last to a location of enhanced $\text{Br}\gamma$ and $\text{Pa}\beta$. All spectra present emission lines [P II] $\lambda 1.1886 \mu\text{m}$, [Fe II] $\lambda\lambda\lambda 1.2570, 1.2946, 1.3209 \mu\text{m}$, and $\text{Pa}\beta\lambda 1.2821 \mu\text{m}$, which can be used to map the kinematics and excitation of the emitting gas.

3 RESULTS

3.1 Stellar populations

The top two panels of Fig. 3 display two examples of fits resulting from the spectral synthesis using the STARLIGHT code. The observed spectra are shown in black, normalized by the flux at $2.1955 \mu\text{m}$ and extracted within apertures of $0''.15 \times 0''.15$. The spectrum of the top panel is centred at the nucleus – defined as the location of the continuum peak – and the one of the lower panel is centred at $1''$ west of the nucleus and is representative of typical extra-nuclear spectra. The best model synthesized via the STARLIGHT code is shown in red. During the fit of the spectra, emission lines and spurious features (e.g. remaining telluric features or bad pixels) were masked out. The grey shaded region in the spectra of Fig. 3 were not synthesized as we do not have observations in the H band.

Using the output from STARLIGHT for each spaxel of the data cube, we constructed maps for the per cent contributions in flux

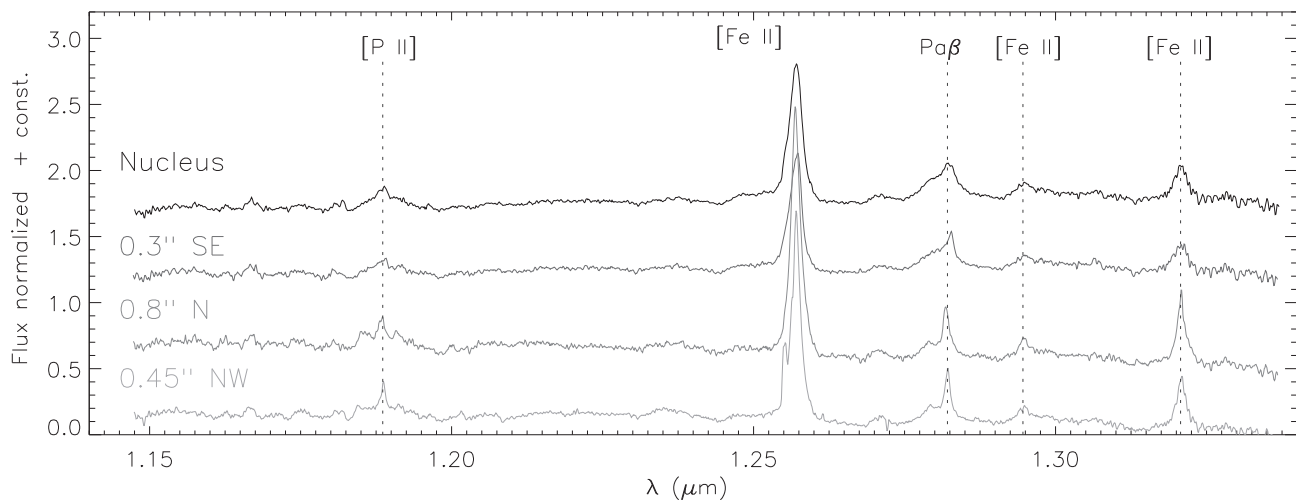


Figure 2. Sample of spectra in the J-band, in arbitrary flux units per wavelength, corrected for Doppler shift, and extracted within a circular aperture of radius $0''.25$. The locations relative to the nucleus are the same for the spectra shown in Fig. 1 of Diniz et al. (2015).

and stellar mass of each stellar population component found in the galaxy spectra. Although the base of components has SSP models for 12 different ages, we binned the contributions into only four age components. This procedure is recommended by Cid Fernandes et al. (2005b) and has been used previously by our group, since the separation of components with very similar ages and metallicities is not well constrained. Therefore, the maps of the stellar population components per cent contribution, weighted by the flux comprise the following age ranges: **young** (x_y : $t \leq 100$ Myr); **young-intermediate** (x_{yi} : $100 < t \leq 700$ Myr); **intermediate-old** (x_{io} : $700 \text{ Myr} < t \leq 2 \text{ Gyr}$) and **old** (x_o : $2 < t \leq 13 \text{ Gyr}$). Similarly, the mass-weighted (m_y, m_{yi}, m_{io}, m_o) component maps were constructed for the same age ranges.

In Fig. 3, we also present the maps for the per cent contributions in flux (middle panels) and mass (bottom panels) of the SPs for NGC 2110. We used the mean per cent deviation over all fitted pixels, defined as $A_{dev} = |O_\lambda - M_\lambda|/O_\lambda$, to exclude regions of poor fits. O_λ is the observed spectrum and M_λ its corresponding best model. Regions with $A_{dev} > 12$ per cent were masked out in the maps and are shown in grey. The cutoff A_{dev} value was determined by eye inspection of the resulting fits. The maps for the young-intermediate population clearly show an increase of contributions with the distance of the nucleus, delineating a ring-shaped structure surrounding the nucleus with a radius of $\sim 1''$. Inside the ring, the old population (right-hand panels) shows flux and mass contributions of up to 70 per cent and 100 per cent, respectively. The intermediate-old population maps do not present significant contributions to the observed fluxes and masses. For the young population a contribution of up to 30 per cent in flux and mass is observed at the nucleus and in some ‘knots’ to the north and north-west of the nucleus at distances $\sim 1''$, thus co-spatial with the ring mentioned above.

Besides the flux and mass contributions of the SPs, the STARLIGHT code outputs also the contributions of the featureless continuum (FC) and BB components to the light at $2.2 \mu\text{m}$. The corresponding maps of these components are shown in Fig. 4, together with maps for the colour excess $[E(B - V)]$ and A_{dev} . In order to construct the map for the BB per cent contribution, we have summed the contributions of all black-body functions in the base. The FC and BB maps show a nuclear unresolved structure, with contributions of up to 10 per cent and 35 per cent, respectively. Such unresolved

structure is expected in AGN considering the spatial resolution of the NIFS data ($0''.15$ or 20 pc), the FC due to continuum emission from the accretion disc and the BB due to emission from the putative dusty torus. The A_{dev} parameter – that measures the quality of the fit – present values smaller than 7 per cent at most locations, indicating the resulting fits reproduce well most of the observed spectra.

3.2 Emission-line flux distribution and gas kinematics

Fig. 5 presents the flux, centroid velocity and velocity dispersion for the following emission lines: $[\text{P II}]\lambda 1.1886 \mu\text{m}$, $[\text{Fe II}]\lambda 1.2570 \mu\text{m}$, $\text{Pa}\beta$ and $\text{H}_2\lambda 2.1218 \mu\text{m}$. These are the strongest NIR emission lines present in the spectra of the nuclear region of NGC 2110. Although Diniz et al. (2015) have already presented the maps for the K-band emission lines, we present again the $\text{H}_2\lambda 2.1218 \mu\text{m}$ maps to allow a comparison of the emission distribution and kinematics of the ionized and molecular gas. We have excluded regions where the measurements have uncertainties larger than 50 per cent in flux and larger than 50 km s^{-1} in the centroid velocity or velocity dispersion. The masked regions are shown in grey in the flux and velocity dispersion maps, and in white in the velocity maps.

The flux distributions of all lines peak at the nucleus, adopted as the location of the continuum peak emission, indicated by a cross in the maps. In order to evidence also the emission of lower flux structures, we have used a logarithmic scale in the maps. These maps show that the flux distributions of distinct emission lines are clearly different from each other. The molecular gas emission is observed over the whole field of view (FOV) presenting two regions of strongest emission, one at the nucleus and other at $\sim 0''.7$ north of it. $\text{Pa}\beta$ shows extended emission mostly along the southeast–northwest direction, similarly to the $\text{Br}\gamma$ flux distribution presented in Diniz et al. (2015). The $[\text{Fe II}]$ flux map presents also a collimated structure, but oriented along the north–south direction. The $[\text{Fe II}]$ emission seems to follow the direction of the radio jet, as indicated by the white contours overlaid to the $[\text{Fe II}]$ flux and σ maps. The radio emission contours are from the 6 cm image of Ulvestad & Wilson (1984), obtained with the Very Large Array (VLA). The white rectangles shown in the $[\text{Fe II}]$ flux and σ maps delineate the FOV of the Keck OSIRIS observations used by Durré & Mould (2014), which will be discussed in Section 4. $[\text{P II}]$ shows a similar

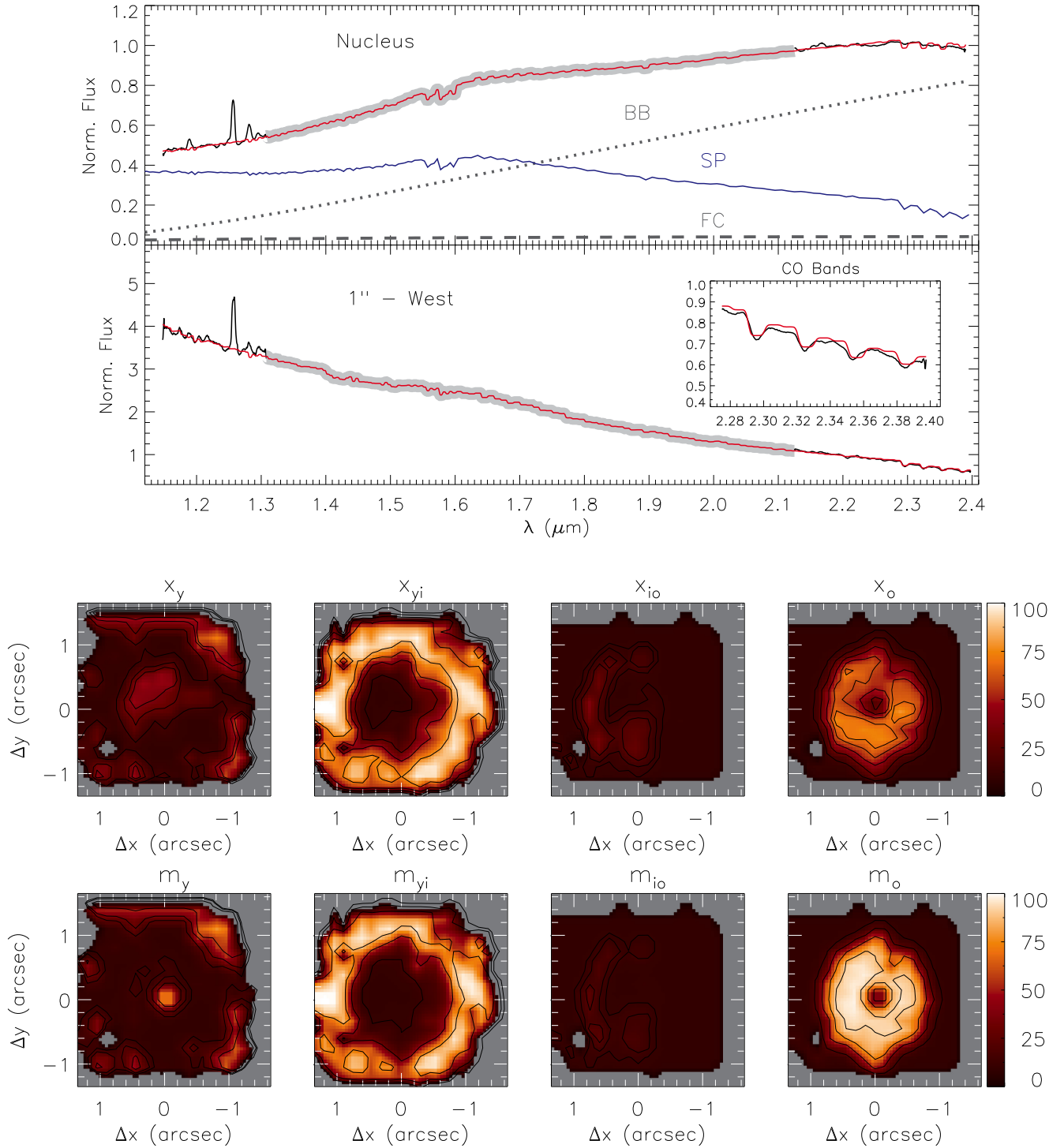


Figure 3. Top two panels: observed spectra from the nucleus and $1''$ west of the nucleus (in black) compared to the synthesized spectra in red. The grey shaded region corresponds to the H-band spectrum that was not observed. The insert shows a zoom of the CO stellar absorption region. For the nucleus, we show the flux contributions of the SP (25 per cent at $2.2 \mu\text{m}$), BB (70 per cent), and FC (5 per cent) components separately. Bottom two row of panels, from left to right: in the top row, per cent contributions to the $2.2 \mu\text{m}$ continuum of young ($x_y \leq 100$ Myr), young-intermediate ($100 < x_{yi} \leq 700$ Myr), intermediate-old ($700 \text{ Myr} < x_{io} \leq 2$ Gyr), and old ($2 < x_o \leq 13$ Gyr) age components; in the bottom row, we show the corresponding per cent mass contributions (m_y , m_{yi} , m_{io} , and m_o).

flux distribution to that $\text{Pa}\beta$, although weaker thus apparently less extended.

The centroid velocity maps are shown in the middle row of panels of Fig. 5. The colour bars show the velocity values in units of

km s^{-1} , relative to the systemic velocity (2332 km s^{-1} , corrected to the heliocentric rest frame), which was determined from the fit of the stellar velocity field (for more details see Diniz et al. (2015)). The H_2 velocity field was already discussed in Diniz et al. (2015)

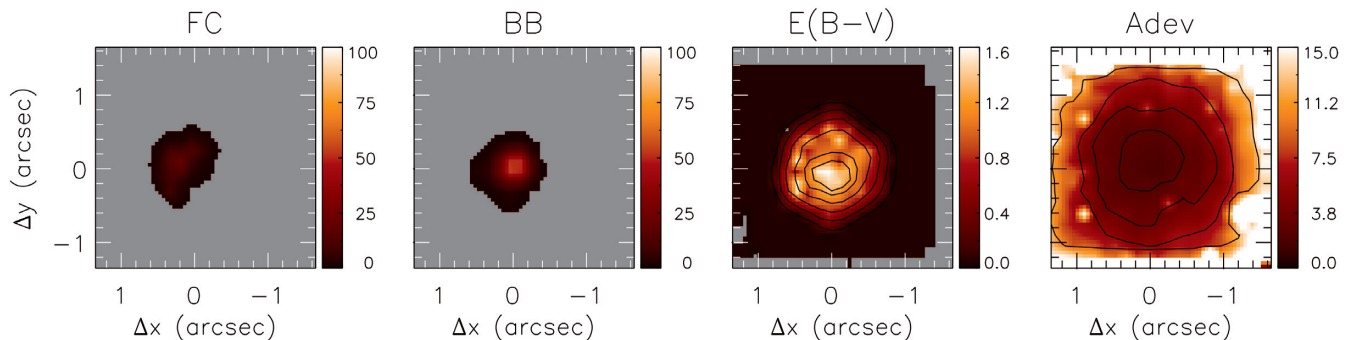


Figure 4. From left to right: per cent flux contributions to the $2.2\ \mu\text{m}$ continuum of the power-law and black-body components; reddening $E(B - V)$ derived from the stellar population synthesis and the parameter A_{dev} , which quantifies the quality of the fit.

and suggest the presence of three components: (i) a rotation pattern with blueshifts to the north and redshifts to the south and a velocity amplitude of $\sim 250\ \text{km s}^{-1}$; this rotation pattern is similar to that seen for the stars (Diniz et al. 2015; Riffel et al. 2017); (ii) gas inflows along nuclear spirals to the north and south of the nucleus and (iii) a compact biconical outflow along the east–west direction, seen within the inner $0''.5$.

The $\text{Pa}\beta$ velocity field is similar to that of $\text{Br}\gamma$ shown in Diniz et al. (2015), but as the line is stronger we were able to fit it over a larger region than for $\text{Br}\gamma$. As for the H_2 , the $\text{Pa}\beta$ velocity field shows blueshifts to the north-west and redshifts to the southeast of the nucleus, which is consistent with rotation in the plane of the galaxy. However, for $\text{Pa}\beta$ the components (ii) and (iii) reported above are not seen. The rotation component seems also to be present in the $[\text{Fe II}]$ velocity field, but this line kinematics shows additional components, such as the blueshifts at the nucleus and redshifts to the east and northeast of the nucleus.

The bottom panels of Fig. 5 show the σ maps. For H_2 , the highest values ($\sim 150\ \text{km s}^{-1}$) are observed at the nucleus and along $\text{PA} \sim 45^\circ/225^\circ$, adjacent from the location of the ‘kinematic spiral’ (systematic residuals relative to a rotation pattern following the shape of spiral arms) seen in the H_2 velocity field (Diniz et al. 2015). The $\text{Pa}\beta$ shows the highest σ values ($\sim 180\ \text{km s}^{-1}$) at the nucleus, while in the extra-nuclear region the values are similar to those of H_2 . Although the $[\text{Fe II}]$ σ map is noisier, as pointed out above, the σ values are similar to those of $\text{Pa}\beta$. The $[\text{Fe II}]$ σ map presents overall higher values, of up to $300\ \text{km s}^{-1}$, with the highest ones seen at the nucleus, while at most locations $\sigma > 150\ \text{km s}^{-1}$.

3.3 Emission-line ratios

In order to investigate the excitation mechanisms of the $[\text{Fe II}]$ emission lines, we constructed the line ratio maps shown in Fig. 6. In each panel, grey regions correspond to masked locations where we were not able to fit one or both lines of the corresponding ratio map, following the same rejection criteria described above. For $[\text{Fe II}] \lambda 1.2570\ \mu\text{m}/\text{Pa}\beta$, the values range from 1 to 10. The highest ones seem to be correlated with the radio contours, while the lowest ones are seen at $\sim 0''.7$ north-west and $\sim 0''.8$ southeast of the nucleus. At the nucleus this ratio is ≈ 6 .

Although the $[\text{Fe II}] \lambda 1.2570\ \mu\text{m}/[\text{P II}] \lambda 1.1886\ \mu\text{m}$ map is noisy, values of up to 30 can be observed, with the highest ones surrounding the radio structures and the lowest ones (≈ 7) at similar locations where the $[\text{Fe II}] \lambda 1.2570\ \mu\text{m}/\text{Pa}\beta$ ratio map also presents its lowest ratios.

The $E(B - V)$ map shown in the right panel of Fig. 6 was constructed using the $\text{Pa}\beta/\text{Br}\gamma$ emission-line ratio, via the following equation:

$$E(B - V) = 4.74 \log \left(\frac{5.88}{F_{\text{Pa}\beta}/F_{\text{Br}\gamma}} \right), \quad (1)$$

where $F_{\text{Pa}\beta}$ and $F_{\text{Br}\gamma}$ are the fluxes of $\text{Pa}\beta$ and $\text{Br}\gamma$ emission lines, respectively. We used the reddening law of Cardelli, Clayton & Mathis (1989) and adopted the intrinsic ratio between $\text{Pa}\beta$ and $\text{Br}\gamma$ of $F_{\text{Pa}\beta}/F_{\text{Br}\gamma} = 5.88$, corresponding to case B at the low-density limit (Osterbrock & Ferland 2006) for an electron temperature of $T_e = 10^4\ \text{K}$. As shown in Diniz et al. (2015), the $\text{Br}\gamma$ emission is detected only in a strip along the north–west–southeast direction. Thus, we map the reddening only at these locations. The corresponding $E(B - V)$ map for NGC 2110 displays the highest values of 2 mag, while the mean $E(B - V)$ value is ≈ 1.4 mag.

4 DISCUSSION

4.1 Distribution of the stellar populations

The distribution of the stellar populations of NGC 2110 (Fig. 3) indicates the old population contributing most to the observed continuum emission within the inner $\approx 0''.8$ ($\approx 120\ \text{pc}$), while the intermediate-age stellar population shows a ring-shaped structure at larger distances from the nucleus. The young stellar population presents the highest flux contributions at the nucleus and close to the borders of the FOV, in the external borders of the ring seen in the intermediate age component.

The presence of an old stellar population around the nucleus of NGC 2110 is in good agreement with previous NIR (Riffel et al. 2009) and optical (González Delgado, Heckman & Leitherer 2001; Raimann et al. 2003) studies. This is also consistent with results found by our group for others Seyfert galaxies – Mrk 1066 (Riffel et al. 2010b), Mrk 1157 (Riffel et al. 2011), NGC 1068 (Storchi-Bergmann et al. 2012) and Mrk 573 (Diniz et al. 2017) – using NIR integral field spectroscopy.

The flux contributions of the young stellar population in the central region of NGC 2110 are co-spatial with locations where the H_2 emission is more intense (Fig. 5). A similar correlation between the young population and the molecular gas distribution was previously observed for NGC 1068 (Storchi-Bergmann et al. 2012), indicating that the molecular gas represents the circumnuclear gas reservoir required for star formation. Based on the J-band continuum image, Durré & Mould (2014) detected four star clusters with estimated ages of 1–3 Myr, surrounding the nucleus

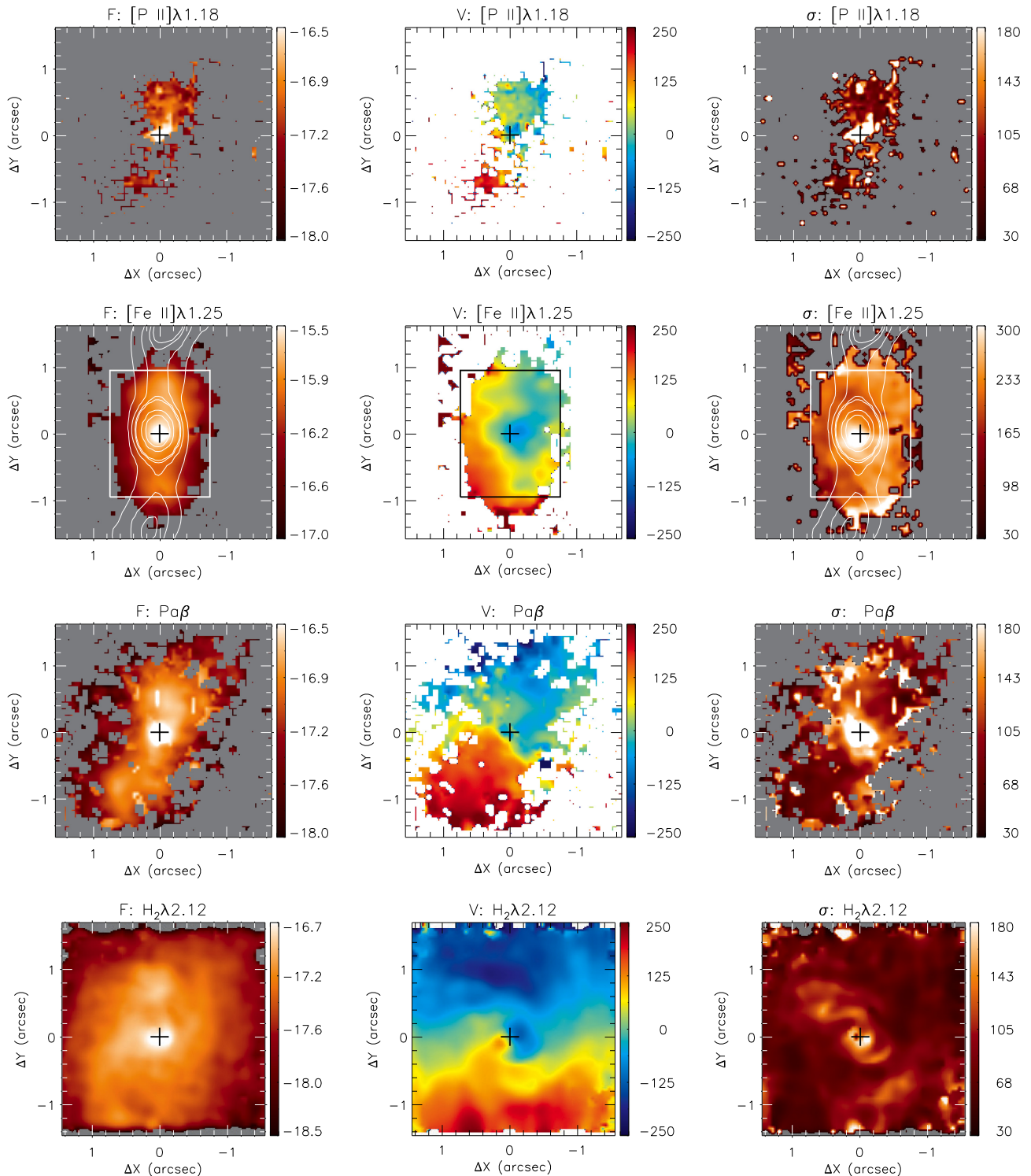


Figure 5. Flux distributions (left-hand panels), velocity fields (middle panels), and velocity dispersion maps (right-hand panels) for the $[\text{P II}]\lambda 1.18 \mu\text{m}$, $[\text{Fe II}]\lambda 1.25 \mu\text{m}$, $\text{Pa}\beta$, and $\text{H}_2\lambda 2.12 \mu\text{m}$ emission lines. The white contours overlaid to the $[\text{Fe II}]$ flux and σ maps are from the 6 cm radio image of Ulvestad & Wilson (1984). White rectangles shown in the $[\text{Fe II}]$ maps indicate the FOV of the observations used by Durré & Mould (2014). The ‘+’ sign marks the location of the nucleus.

of NGC 2110 at distances smaller than $0''.2$. Our J-band continuum (Fig. 7 emission image constructed from the NIFS data cube in the same spectral range (1.228–1.289 μm) used by them, does not show any clear knot of emission associated to the unresolved regions seen in their continuum image. The discrepancy between OSIRIS and

NIFS continuum images is possible due to a slightly better angular resolution of the OSIRIS data. On the other hand, a young stellar population component is found in our spectral synthesis (Fig. 3), but it should be noted that our spectral base does not include SSP components younger than 10 Myr. Furthermore, reddened young

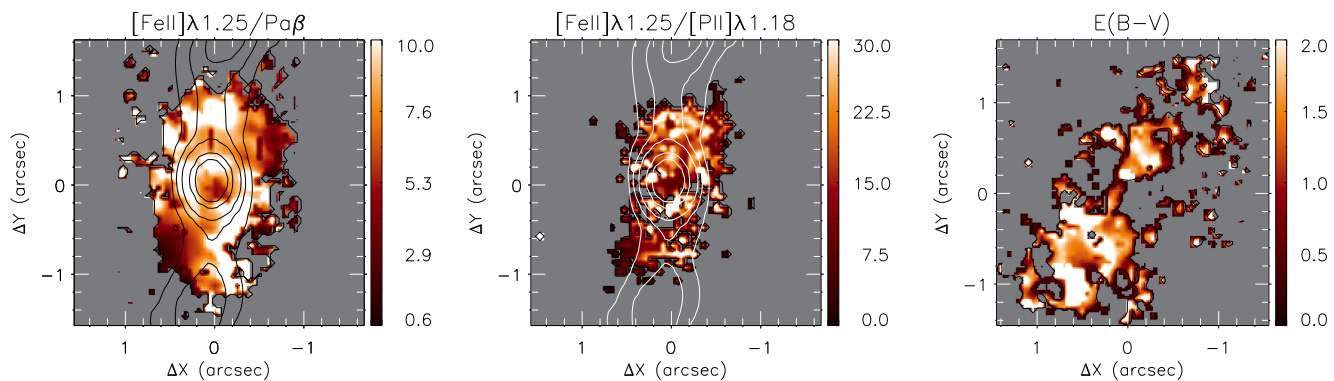


Figure 6. $[\text{Fe II}]\lambda 1.25 \mu\text{m}/\text{Pa}\beta$ line ratio map (left-hand panel), $[\text{Fe II}]\lambda 1.25 \mu\text{m}/[\text{P II}]\lambda 1.18 \mu\text{m}$ line ratio map (centre panel) and reddening map obtained from the $\text{Pa}\beta/\text{Br}\gamma$ line ratio (right-hand panel). The contours shown in the first two maps trace the radio emission.

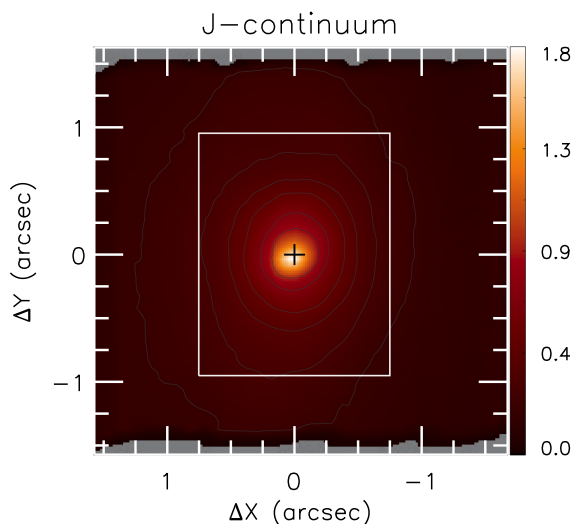


Figure 7. J-band continuum image obtained by averaging the NIFS data cube in the spectral range $1.228\text{--}1.289 \mu\text{m}$. The colour bar shows the fluxes in units of $10^{-17} \text{erg s}^{-1} \text{cm}^{-2} \text{\AA}^{-1}$. The white rectangle corresponds to the FOV of the observations used by Durré & Mould (2014).

stars of age of a few million years are indistinguishable from an FC component.

The 150 pc radius ring-shaped structure observed in the young-intermediate stellar population component both in flux and mass seems to be weakly correlated with the lowest stellar velocity dispersion (σ_*) values presented in Diniz et al. (2015) and Riffel et al. (2017). Similar rings of young/intermediate-age stellar populations associated to low σ_* have been previously reported by our group for other Seyfert galaxies (Riffel et al. 2010b, 2011; Diniz et al. 2017; Dametto et al. 2019), suggesting that this may be a frequent characteristic of the central region of AGN. A possible scenario for this is: if there is plenty of gas moving towards the central region of the galaxy, this gas may find suitable conditions for the formation of new stars in the inner few 100 pc. Part of this gas will continue falling towards the centre, and/or the mass loss from the recently formed massive stars will move inwards triggering and feeding an AGN there. Low σ_* rings, seen in the central region of AGNs would thus be originated in intermediate-age stars, which have formed from low-velocity dispersion gas, tracing the cold kinematics of the gas cloud that formed them (Riffel et al. 2017).

Flux and mass contribution maps of each stellar population component (Fig. 3) show that the old population contributes most inside the young-intermediate age ring, while the young stellar component is found within $\approx 0''.5$ (~ 70 pc) from the nucleus and also at the outer borders of the ring.

4.2 Extinction

The average reddening value for the gas (right panel of Fig. 6) is $E(B - V) \sim 1.4$ mag, while for the stars (third panel of Fig. 4) $E(B - V) \sim 0.8$ mag. In fact, a larger reddening is expected for the gas than for the stars, since the former should be concentrated in the galactic disc, while the stars reach higher latitudes in the galaxy bulge, where the reddening is lower (Calzetti, Kinney & Storchi-Bergmann 1994).

Our $E(B - V)$ map for the gas is in good agreement with previous estimates using the $[\text{Fe II}] \lambda 1257/\lambda 1644$ flux ratio (Durré & Mould 2014) and using the $\text{Pa}\beta$ and $\text{Br}\gamma$ fluxes (Storchi-Bergmann et al. 1999) from long-slit spectra.

The stellar $E(B - V)$ values obtained by us are larger than those obtained by Raimann et al. (2003) (~ 0.4 mag) using optical observations, but they are consistent with those reported by Riffel et al. (2009) (~ 0.6 mag) from NIR data. Higher reddening values determined using NIR data as compared to those using optical determinations can be interpreted as due to the fact that NIR observations are less affected by dust extinction and thus probe more obscured regions immersed in the plane of the galaxy (Martins et al. 2013; Riffel et al. 2015a).

4.3 Hot dust emission and AGN Featureless continuum

Our synthesis results detected a small contribution (10 per cent) of the power-law FC component, which is associated with the radiation from the accretion disc. Although the FC component is expected to be more important at shorter wavelengths, it is usually necessary to properly fit the NIR spectral energy distribution as well. Riffel et al. (2009) presented spectral synthesis of the nuclear NIR spectra of a sample of 24 Seyfert galaxies and found that at least 50 per cent of the Seyfert 2 and 60 per cent of the Seyfert 1 require a power-law component to properly fit their spectra. For NGC 2110, they found a contribution of $\text{FC} = 33.6$ per cent to the flux at $1.2 \mu\text{m}$, which translates to about 13 per cent at $2.2 \mu\text{m}$ (our normalization point). Thus, our result is in good agreement with those of Riffel et al. (2009).

We found that the hot dust emission, traced by the BB component, contributes with 35 per cent of the $2.2 \mu\text{m}$ unresolved nuclear

continuum emission. This value is larger than that found by Riffel et al. (2009) of only 1 percent at 1.2 μm . In addition, the spatial resolution of our data is about one order of magnitude better than those of Riffel et al. (2009), which allow us to better probe the unresolved dust emission. Similar discrepancies of the nuclear contributions of BB components between high and low resolution data have already been reported for other objects (e.g. Riffel et al. 2010b). To determine the average dust temperature, we fitted an integrated spectrum extracted within an 0.3 radius aperture centred at the peak of the continuum emission. Three dust components were used by STARLIGHT in the fit (with temperatures of 1200, 1300, and 1400 K) and the resulting dust temperature is ~ 1340 K, obtained by computing an average temperature weighted by the integrated flux contribution of each component.

From the contributions of the BB components to the observed continuum we can estimate the mass of the hot dust that originates these components. The total mass of hot dust (M_{HD}) at the nucleus of NGC 2110 was estimated following Riffel et al. (2009), using the formalism of Barvainis (1987) and assuming the dust composed by grains of graphite.

The IR spectral luminosity of each dust grain, in $\text{erg s}^{-1} \text{Hz}^{-1}$, can be written as

$$L_{\nu, \text{ir}}^{\text{gr}} = 4\pi^2 a^2 Q_{\nu} B_{\nu}(T_{\text{gr}}), \quad (2)$$

where $a = 0.05 \mu\text{m}$ is the grain radius, $Q_{\nu} = 1.4 \times 10^{-24} \nu^{1.6}$ is its absorption efficiency, and $B_{\nu}(T_{\text{gr}})$ is its spectral distribution assumed to be a Planck function for a temperature T_{gr} .

The total number of graphite grains can be obtained from

$$N_{\text{HD}} \sim \frac{L_{\text{ir}}^{\text{HD}}}{L_{\text{ir}}^{\text{gr}}}, \quad (3)$$

where $L_{\text{ir}}^{\text{HD}}$ is the total luminosity of the hot dust, obtained by integrating the flux of each BB component contribution from the synthesis. Then, we multiplied the integrated normalized flux by the normalization flux at 2.1955 μm , and converted it to the correct units. In order to obtain $L_{\text{ir}}^{\text{gr}}$, we have integrated the equation (2) for all temperatures, ranging them from 700 to 1400 K, in steps of 100 K.

Under these assumptions, M_{HD} can be obtained by (e.g. Rodríguez-Ardila, Contini & Viegas 2005a):

$$M_{\text{HD}} \sim \frac{4\pi}{3} a^3 N_{\text{HD}} \rho_{\text{gr}}, \quad (4)$$

where $\rho_{\text{gr}} = 2.26 \text{ g cm}^{-3}$ is the density of the grain. The total dust mass estimated for the nucleus of NGC 2110 is $M_{\text{HD}} \sim 3 \times 10^{-2} M_{\odot}$, which is within the range of masses obtained for other active galaxies ($10^{-4} - 10^{-1} M_{\odot}$) (e.g. Rodríguez-Ardila, Contini & Viegas 2005a; Rodríguez-Ardila & Mazzalay 2006; Riffel et al. 2009, 2009a; Diniz et al. 2018).

4.4 Gas excitation

A widely studied issue in the NIR is how to determine the main mechanism that originates the lines of [Fe II] and H_2 . In Diniz et al. (2015) we conclude that the H_2 emission is due to thermal processes (heating of the gas by X-rays from the AGN and/or shocks), with an excitation temperature in the range $\sim 2100 - 2700$ K. Here, we discuss the origin of the [Fe II] emission.

The [Fe II] emission lines can be produced by collisional excitation due to the heating of the gas by shocks (Hollenbach & McKee 1989) or by X-rays from the AGN (Maloney, Hollenbach & Tielens 1996). The key point is to determine whether the excitation

of [Fe II] is due to X-rays or shocks. As pointed out in Section 3.2, the kinematics of the [Fe II] emitting gas reveals a distorted velocity field, higher σ values and the flux distribution correlated with the radio jet, supporting the contribution of shocks to the [Fe II] emission (see Section 4.5 for more details on the interpretation of the gas kinematics).

One way to investigate the origin of [Fe II] is using emission-line ratios, such as [Fe II] λ 1.2570 μm /Pa β and [Fe II] λ 1.2570 μm /[P II] λ 1.1886 μm . The [Fe II]/Pa β line ratio presents values between 0.6 and 2 for Seyfert nuclei, lower than 0.6 for Starbursts, and higher than 2 for Low-ionization nuclear emission-line regions (LINERs) (Reunanen, Kotilainen & Prieto 2002; Rodríguez-Ardila et al. 2004, 2005b; Riffel et al. 2013; Colina et al. 2015). The [Fe II]/Pa β ratio map (left panel of Fig. 6) presents values higher than 2 for most of the observed field, with the highest ones being co-spatial or surrounding the radio structure. This suggests that the radio jet plays an important role in the origin of the [Fe II] emission.

The conclusion above is also supported by the [Fe II] λ 1.2570 μm /[P II] λ 1.1886 μm map shown in the central panel of Fig. 6. These lines have similar ionization temperatures, with their parent ions presenting similar ionization potentials and radiative recombination coefficients. In H II regions, where shocks are not important, the [Fe II]/[P II] ratio is ~ 2 . For supernova remnants, where shocks are the dominant excitation mechanism, line ratios are typically larger than 20 (Oliva et al. 2001). In this case, fast shocks have passed through the gas destroying the dust grains, releasing the Fe and thus enhancing its abundance and its emission. The same can happen in the central region of active galaxies, where nuclear jets can produce shocks (e.g. Oliva et al. 2001; Storchi-Bergmann et al. 2009). For NGC 2110, [Fe II]/[P II] values reach up to 30, being observed at the same locations of the highest [Fe II]/Pa β ratios, supporting the contribution of shocks to the emission of the [Fe II] line. Thus, based on the observed emission-line ratios, as well as on the correlation among the σ values, flux distribution and the radio structure, we conclude that the main excitation mechanism of [Fe II] in NGC 2110 are shocks produced by the interaction of the radio jet with the ambient gas.

Rosario et al. (2010) have concluded that the radio jet escapes the disc towards high latitudes and a direct interaction of the gas near the plane of the galaxy with the radio jet would be unlikely. However, the spatial resolution of our data (~ 30 pc) is better than theirs, resolving structures smaller than the disc scale height. We have thus apparently been able to probe this interaction via the [Fe II] emitting line. Our proposed scenario is thus that the radio jet is pushing away gas from the disc of the galaxy in the vicinity of the AGN, launching it to larger latitudes above the plane of the galaxy.

4.5 Gaseous kinematics

Previous studies of NGC 2110 at optical and NIR wavelengths have shown a complex gas kinematics in the central region of the galaxy. Asymmetries in the rotation curve of the galaxy and distinct kinematic components have been observed (e.g. Storchi-Bergmann et al. 1999; Knop et al. 2001; González Delgado et al. 2002; Ferruit et al. 2004; Schnorr-Müller et al. 2014; Diniz et al. 2015). In Diniz et al. (2015) we found that the H_2 emitting gas shows three distinct kinematic components: gas rotation in the plane of the disc, streaming motions towards the centre along nuclear spiral arms and a compact outflow within the inner 70 pc oriented along the east–west projected direction. The disc component and the compact

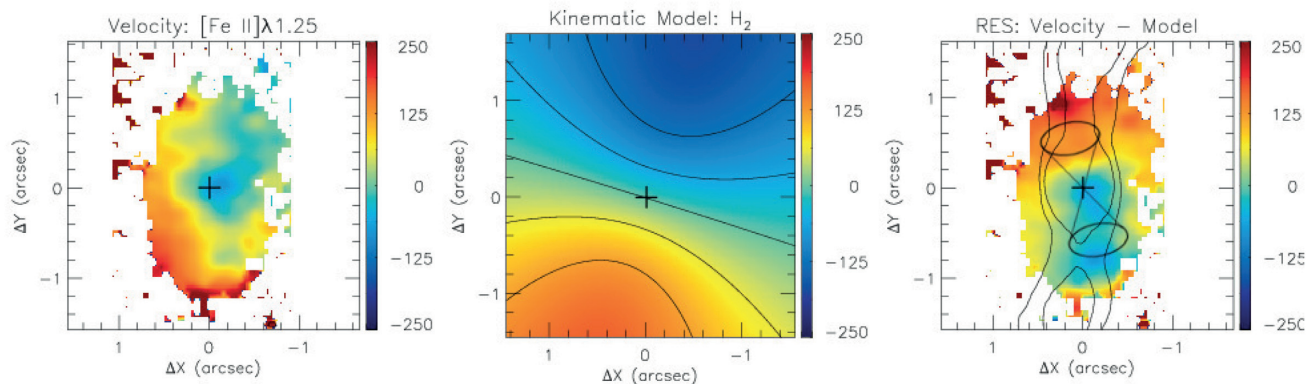


Figure 8. Observed velocity field for the [Fe II] (left), rotating disc model for the H₂ from Diniz et al. (2015) (middle) and residual map obtained by the subtraction of the model from the observed [Fe II] velocity field (right). The conical shape drawn at the right panel represents the adopted geometry used to estimate the mass-outflow rate.

outflow are also observed using optical IFS (Schnorr-Müller et al. 2014), which reveals also a warm – higher velocity dispersion – disc and a high-latitude cloud observed in blueshift at 1′′5–4′′ north of the nucleus.

Although all velocity fields of the emitting gas (Fig. 5) show an overall similar rotation pattern, with blueshifts to the north-west and redshifts to the southeast, it can be clearly seen that distinct emission lines present somewhat distinct kinematics. The σ maps show that at most locations the H₂ presents the lowest σ values, followed by Pa β and [P II], with [Fe II] presenting the highest values, which seem to be correlated with the radio emission. The velocity field of the molecular gas – already discussed in Diniz et al. (2015) – is completely distinct from that of the ionized gas, and differences between the velocity fields for the [Fe II] and H recombination lines are also clearly present.

The Pa β kinematics is similar to that of Br γ from Diniz et al. (2015) and consistent with the presence of the warm gas disc component detected by Schnorr-Müller et al. (2014). The velocity fields are dominated by rotation in the galaxy disc and their emission can be attributed as being due to the heating and ionization of the gas by the AGN radiation.

Comparing our [Fe II] λ 1.2570 μ m kinematic maps with those obtained by Durré & Mould (2014) for the same emission line, we find that they are consistent each to other, considering that the spatial orientation of the maps originally published is incorrect. Their maps are rotated by 90°, to have the north–south direction along the y-axis (Durré, M., private communication). Considering this, it can be noticed that both their and our σ maps show a correlation with the radio structure, which is clearly observed as enhanced σ values surrounding the radio structure. It is worth noticing that our [Fe II] kinematics is similar to that of the [N II] nuclear component detected by Schnorr-Müller et al. (2014), although the spatial resolution of our data is about 5 times better than theirs. Recently, Rosario et al. (2019) presented the Atacama Large Millimeter Array (ALMA), Hubble and Spitzer Space Telescopes, and the Very Large Telescope/SINFONI observations of NGC 2110 and found that the cold molecular gas presents a lacuna co-spatial with the highest emission of ionized and hot molecular gas, indicating that the AGN is directly influencing the properties of the cold molecular gas. In summary, we have found that: (i) the [Fe II] emission is oriented along the radio jet; (ii) its velocity dispersion map shows enhanced values surrounding the radio structures; (iii) the emission-line ratios support the presence of shocks and (iv) the [Fe II] velocity field shows distortions relative to a rotating disc. Considering all this,

we suggest that besides rotation, the [Fe II] kinematics supports the presence of an additional outflowing component due to the interaction of the radio jet with the ambient gas. The interaction of the radio jet with the ambient gas is supported by its observed orientation (which is displaced by 29° from the major axis of the galaxy and inclined by 40° relative to the plane of the sky, Pringle et al. 1999), supporting an interception with the disc of the galaxy for typical disc scale heights. This is also consistent with the CO emission distribution presented by Rosario et al. (2019) and similar results for the gas kinematics have been observed also for other Seyfert galaxies (e.g. Ferruit et al. 1999; Riffel et al. 2006; Rosario et al. 2010; Riffel, Storchi-Bergmann & Riffel 2015b).

4.5.1 The mass outflow rate

Aiming to isolate the outflowing gas component in the [Fe II] kinematics, we have used the rotating disc model for the molecular gas (which is dominated by rotation) presented in Diniz et al. (2015) to construct a residual map between the observed [Fe II] kinematics and this model under the assumption that the rotation component should be similar for both gas species. Fig. 8 presents the [Fe II] λ 1.2570 μ m velocity field (left-hand panel), the rotating disc model for the H₂ (middle panel) and the residual map (right-hand panel). Contours from the radio image are overlaid on the residual map.

The residual map clearly shows excess blueshifts at the nucleus and to the south and redshifts to the north, with absolute values of up to 200 km s⁻¹, mainly oriented along the radio structure. These residuals, together with the correlation of the [Fe II] λ 1.2570 μ m fluxes, σ values and line ratios with the radio structure lead us to interpret that the residuals are tracing a biconical outflow possibly originated from interaction of the radio jet with the [Fe II] emitting gas. This conclusion is supported by previous studies of other similar objects, which have shown the [Fe II] has a more disturbed kinematics than the molecular and atomic hydrogen, being considered a tracer of the AGN feedback (e.g. Hicks et al. 2009; Müller-Sánchez et al. 2009; Rosario et al. 2010; Storchi-Bergmann et al. 2010; Riffel et al. 2015b).

We estimate the ionized gas mass outflow rate through a circular cross-section with radius $r = 0''.25$ (~ 36 pc) at a distance of $h = 0''.5$ (~ 73 pc) from the nucleus, using

$$\dot{M}_{\text{out}} = 2 m_p N_e v_{\text{out}} f \pi r^2, \quad (5)$$

where m_p is the proton mass, N_e is the electron density, v_{out} is the velocity of the outflowing gas ($v_{\text{out}} = v_{\text{obs}} / \sin \theta$), f is the filling factor and θ is the angle between the axis of the cone and the plane of sky. We have assumed $N_e = 500 \text{ cm}^{-3}$ which is a typical value for outflowing regions around Seyfert nuclei as derived using long-slit spectroscopy (e.g. Dors et al. 2014), $f = 0.01$ (which is a value commonly used for other Seyfert galaxies – Storchi-Bergmann et al. (e.g. 2010); Schnorr-Müller et al. (e.g. 2014)) and $v_{\text{out}} = 80 \text{ km s}^{-1} / \sin \theta$ (value obtained from the residual map of Fig. 8). Pringle et al. (1999) have derived the orientation of the radio jet as being 50° in relative to the line of sight and therefore $\theta = 40^\circ$.

The ionized gas mass outflow rate obtained under the assumptions above is $\dot{M}_{\text{out}} \approx 0.5 M_\odot \text{ yr}^{-1}$, being similar to the value obtained by Schnorr-Müller et al. (2014) using optical observations, of $\approx 0.9 M_\odot \text{ yr}^{-1}$, although these authors could not clearly resolve the geometry of the outflow due to their lower angular resolution. The obtained mass outflow rate is within the range of values obtained in previous studies of similar low-luminosity Seyfert and LINER galaxies (e.g. Veilleux, Cecil & Bland-Hawthorn 2005; Crenshaw & Kraemer 2007; Barbosa et al. 2009; Storchi-Bergmann et al. 2010; Riffel, Storchi-Bergmann & Riffel 2015b).

The mass outflow rate can also be compared to that of a compact outflow seen in hot molecular hydrogen, which is 1200 times lower, but this is because the hot molecular gas emission traces only a small fraction of the total content of molecular gas (Dale et al. 2005; Müller-Sánchez et al. 2006; Mazzalay et al. 2013). In any case, we note that the molecular gas outflow is oriented perpendicularly to the outflow observed in [Fe II] and thus seem to have distinct origin. As already discussed in Storchi-Bergmann et al. (2009), the [Fe II] is a better tracer of AGN driven outflows than the [N II], [S II] and even the H recombination lines.

Following Storchi-Bergmann et al. (2010), we can use the above mass outflow rate to estimate the kinetic power of the outflow by

$$\dot{E} \approx \frac{\dot{M}_{\text{out}}}{2} (v_{\text{out}}^2 + \sigma^2), \quad (6)$$

where $v_{\text{out}} = v_{\text{obs}} / \sin 40^\circ$ is the velocity of the outflowing gas and σ its velocity dispersion. Using $\sigma \approx 250 \text{ km s}^{-1}$ (from Fig. 5), and $v_{\text{out}} \approx 125 \text{ km s}^{-1}$, we obtain $\dot{E} \approx 1.3 \times 10^{40} \text{ erg s}^{-1}$. The bolometric luminosity of NGC 2110 is $L_{\text{bol}} = 2.9 \times 10^{43} \text{ erg s}^{-1}$ (Schnorr-Müller et al. 2014), thus the kinetic power is three orders of magnitude lower than L_{bol} . This value is similar to those obtained for other similar targets and somewhat larger than those obtained by Barbosa et al. (2009) for 6 nearby Seyfert galaxies, which are in the range $10^{-5} \leq \dot{E} / L_{\text{bol}} \leq 10^{-4}$.

Therefore, only a small fraction of the mass accretion rate of $5 \times 10^{-3} M_\odot \text{ yr}^{-1}$ (Schnorr-Müller et al. 2014) – necessary to power the AGN at the nucleus of NGC 2110 – is transformed into kinetic power in the outflow.

This kinetic power is lower than the threshold suggested by galaxy evolution models, above which the feedback is strong enough to influence the evolution of the host galaxy (Di Matteo, Springel & Hernquist 2005).

Although having concluded that the power of the outflow is low, our data allowed us to conclude that shocks due to the interaction of the radio jet with the galaxy circumnuclear interstellar medium play an important role both in the kinematics and in the emission and excitation of the [Fe II] line. This is consistent with previous results from literature obtained for the central region of NGC 2110. Storchi-Bergmann et al. (1999), Knop et al. (2001), and Ferruit et al. (2004) reported that the [Fe II] line exhibits a much broader and more complex profile than the H_2 , being this broadening attributed to fast

shocks resulting from interaction between the radio jet and the gas in its vicinity.

5 CONCLUSIONS

We have mapped the stellar population, emission-line flux distribution, gas excitation and kinematics of the inner 200 pc of the Seyfert 2 galaxy NGC 2110, using NIR J- and K-band integral field spectroscopy at a spatial resolution of $\sim 22 \text{ pc}$. This paper represents a continuing study of Diniz et al. (2015), where we mapped the molecular gas and stellar kinematics of the nuclear region of NGC 2110. The main results of this paper are listed below.

(i) The young-intermediate age stellar population contribution is dominant in a ring-like structure at $\sim 140 \text{ pc}$ from the nucleus. Similar structures have been found for other galaxies associated to low stellar velocity dispersion rings, leading to the conclusion that such rings are originated in stellar populations of ages between 100 Myr and 1 Gyr;

(ii) The distribution of the oldest stellar population dominates the inner $\sim 130 \text{ pc}$, inside the ring;

(iii) The distribution of the young stellar population (with contributions of up to 30 percent of the continuum emission) is seen in the inner 0.5 (70 pc), being co-spatial with regions of enhanced H_2 emission, indicating that the molecular gas represents the circumnuclear gas reservoir required for star formation; some recent star formation is also seen at a few locations at the external borders of the ring;

(iv) Besides the contributions of the stellar populations, the nuclear region requires additional components to fit the continuum: a FC component represented by a power-law and a hot dust component (from the dusty torus) represented by black-body components, contributing with 10 percent and 35 percent, respectively, to the flux at $2.2 \mu\text{m}$. The estimated mass of hot dust in the nucleus is $\sim 0.03 M_\odot$;

(v) The emission line flux distributions are distinct from each other. The H_2 emission is distributed over the whole field of view, while the H recombination lines emission is more extended along $\text{PA} \sim -30^\circ$. The [Fe II] emission is more extended along the north–south direction, being co-spatial with the radio emission;

(vi) Based on emission-line ratios and the comparison of the [Fe II] kinematics with the radio emission, we conclude that most of the [Fe II] emission is produced by shocks due to the interaction of the radio jet with the ambient gas;

(vii) Distinct kinematic components are seen for distinct emission lines. The H_2 kinematics shows a rotating disc component, a compact equatorial outflow within the inner 70 pc and inflows along spiral arms. The [Fe II] kinematics, besides presenting also the rotating disc component, shows also a biconical outflow oriented along the north–south direction, following the direction of the radio jet;

(viii) Further evidence of interaction of the radio jet with the [Fe II] emitting gas are: an enhancement in the σ values and line ratio values indicating shock excitation in regions surrounding the radio jet;

(ix) Using a kinematic model for the rotating disc component derived from the molecular gas kinematics and subtracting it from the [Fe II] velocity field, we were able to isolate the outflow component. We derive an ionized gas mass outflow rate in this component of $\dot{M}_{\text{out}} \approx 0.5 M_\odot \text{ yr}^{-1}$ at a distance of $\sim 70 \text{ pc}$ from the nucleus;

(x) The kinetic power of the outflow is $1.3 \times 10^{40} \text{ erg s}^{-1}$ and is less than 0.05 percent of the bolometric luminosity of the AGN in

NGC 2110, implying little influence of the corresponding feedback in the evolution of the galaxy.

ACKNOWLEDGEMENTS

We thank the referee, Dr. Mark Durré, for valuable comments which helped to improve this paper. Based on observations obtained at the Gemini Observatory, which is operated by the Association of Universities for Research in Astronomy, Inc., under a cooperative agreement with the NSF on behalf of the Gemini partnership: the National Science Foundation (United States), the Science and Technology Facilities Council (United Kingdom), the National Research Council (Canada), CONICYT (Chile), the Australian Research Council (Australia), Ministério da Ciência e Tecnologia (Brazil) and South-EastCYT (Argentina). This research has made use of the NASA/IPAC Extragalactic Database (NED) which is operated by the Jet Propulsion Laboratory, California Institute of Technology, under contract with the National Aeronautics and Space Administration.

This study was financed in part by the Coordenação de Aperfeiçoamento de Pessoal de Nível Superior - Brasil (CAPES) - Finance Code 001, Conselho Nacional de Desenvolvimento Científico e Tecnológico (CNPq) and Fundação de Amparo à pesquisa do Estado do RS (FAPERGS).

REFERENCES

- Asari N. V., Cid Fernandes R., Stasińska G., Torres-Papaqui J. P., Mateus A., Sodré L., Schoenell W., Gomes J. M., 2007, *MNRAS*, 381, 263
- Barbosa F. K. B., Storch-Bergmann T., Cid Fernandes R., Winge C., Schmitt H., 2009, *MNRAS*, 396, 2
- Barvainis R., 1987, *ApJ*, 320, 537
- Blietz M., Cameron M., Drapatz S., Genzel R., Krabbe A., van der Werf P., 1994, *ApJ*, 421, 92
- Bower R. G., Benson A. J., Malbon R., Helly J. C., Frenk C. S., Baugh C. M., Cole S., Lacey C. G., 2006, *MNRAS*, 370, 645
- Calzetti D., Kinney A. L., Storch-Bergmann T., 1994, *ApJ*, 429, 582
- Cardelli J. A., Clayton G. C., Mathis J. S., 1989, *ApJ*, 345, 245
- Cid Fernandes R., Gu Q., Melnick J., Terlevich E., Terlevich R., Kunth D., Rodrigues Lacerda R., Joguet B., 2004, *MNRAS*, 355, 273
- Cid Fernandes R., Mateus A., Sodré L., Stasińska G., Gomes J. M., 2005a, *MNRAS*, 358, 363
- Cid Fernandes R., González Delgado R. M., Storch-Bergmann T., Martins L. Pires, Schmitt H., 2005b, *MNRAS*, 356, 270
- Colina L. et al., 2015, *A&A*, 578, 48
- Crenshaw D. M., Kraemer S. B., 2007, *ApJ*, 659, 250
- Crenshaw D. M., Kraemer S. B., Gabel J. R., 2003, *AJ*, 126, 1690
- Dahmer-Hahn L. G. et al., 2019, *MNRAS*, 482, 5211
- Dale D. A., Sheth K., Helou G., Regan M. W., Hüttemeister S., 2005, *AJ*, 129, 2197
- Dametto N. Z., Riffel R., Pastoriza M. G., Rodríguez-Ardila A., Hernandez-Jimenez J. A., Carvalho E. A., 2014, *MNRAS*, 443, 1754.D
- Dametto N. Z. et al., 2019, *MNRAS*, 482, 4437
- Das V., Crenshaw D. M., Hutchings J. B., Deo R. P., Kraemer S. B., Gull T. R., Kaiser M. E., Nelson C. H., Weistrop D., 2005, *AJ*, 130, 945
- Das V., Crenshaw D. M., Kraemer S. B., Deo R. P., 2006, *AJ*, 132, 620
- Davies R. I., Maciejewski W., Hicks E. K. S., Tacconi L. J., Genzel R., Engel H., 2009, *ApJ*, 702, 114D
- Di Matteo T., Springel V., Hernquist L., 2005, *Nature*, 433, 604
- Diniz M. R., Riffel R. A., Storch-Bergmann T., Winge C., 2015, *MNRAS*, 453, 1727
- Diniz M. R., Riffel R. A., Riffel R., Crenshaw D. M., Storch-Bergmann T., Fischer T. C., Schmitt H. R., Kraemer S. B., 2017, *MNRAS*, 469, 3286.
- Diniz M. R., Riffel R. A., Dors O. L., 2018, *RNAAS*, 2, 3
- Dors O. L., Cardaci M. V., Hägele G. F., Krabbe A. C., 2014, *MNRAS*, 443, 1291
- Durré M., Mould J., 2014, *ApJ*, 784, 79
- Emsellem E., Greusard D., Combes F., Friedli D., Leon S., Pécontal E., Wozniak H., 2001, *A&A*, 368, 52
- Fathi K., van de Ven G., Peletier R. F., Emsellem E., Falcón-Barroso J., Cappellari M., de Zeeuw T., 2005, *MNRAS*, 364, 773
- Ferruit P., Wilson A. S., Whittle M., Simpson C., Mulchaey J. S., Ferland G., 1999, *ApJ*, 523, 147.
- Ferruit P., Mundell C. G., Nagar N. M., Emsellem E., Pécontal E., Wilson A. S., Schinnerer E., 2004, *MNRAS*, 352, 1180
- Forbes D. A., Ward M. J., 1993, *ApJ*, 416, 150
- González Delgado R. M., Heckman T., Leitherer C., 2001, *ApJ*, 546, 845
- González Delgado R. M., Arribas S., Pérez E., Heckman T., 2002, *ApJ*, 579, 188
- Hennig M. G., Riffel R. A., Dors O. L., Riffel R., Storch-Bergmann T., Colina L., 2018, *MNRAS*, 477, 1086
- Hicks E. K. S., Davies R. I., Malkan M. A., Genzel R., Tacconi L. J., Sánchez F. M., Sternberg A., 2009, *ApJ*, 696, 448
- Hollenbach D., McKee C. F., 1989, *ApJ*, 342, 306
- Hopkins P. F., Hayward C. C., Narayanan D., Hernquist L., 2012, *MNRAS*, 420, 320
- Imanishi M., Dudley C. C., 2000, *ApJ*, 545, 701
- Knapen J. H., Shlosman I., Peletier R. F., 2000, *ApJ*, 529, 93
- Knop R. A., Armus L., Matthews K., Murphy T. W., Soifer B. T., 2001, *AJ*, 122, 764
- Maciejewski W., Teuben P. J., Sparke L. S., Stone J. M., 2002, *MNRAS*, 329, 502
- Maloney P. R., Hollenbach D. J., Tielens A. G. G. M., 1996, *ApJ*, 466, 561
- Maraston C., 2005, *MNRAS*, 362, 799
- Markwardt C. B., 2009, in Bohlender D. A., Durand D., Dowler P., eds, *Astronomical Society of the Pacific Conference Series*. Vol. 411, Quebec, Canada, p. 251
- Martins L. P., Rodríguez-Ardila A., Diniz S., Gruenwald R., de Souza R., 2013, *MNRAS*, 431, 1823
- Mazzalay X. et al., 2013, *MNRAS*, 428, 2389
- McGregor P. J. et al., 2003, *Proceedings of the SPIE*, 4841, 1581
- Morgan W. W., 1958, *PASP*, 70, 364
- Müller-Sánchez F., Davies R. I., Eisenhauer F., Tacconi L. J., Genzel R., Sternberg A., 2006, *A&A*, 454, 492
- Müller-Sánchez F., Davies R. I., Genzel R., Tacconi L. J., Eisenhauer F., Hicks E. K. S., Friedrich S., Sternberg A., 2009, *ApJ*, 691, 749
- Oliva E. et al., 2001, *A&A*, 369, L5
- Osterbrock D. E., Ferland G. J., 2006, *Astrophysics of Gaseous Nebulae and Active Galactic Nuclei*, 2nd edn. University Science Books, Mill Valley, California
- Pringle J. E., Antonucci R. R. J., Clarke C. J., Kinney A. L., Schmitt H. R., Ulvestad J. S., 1999, *ApJ*, 526, L9
- Raimann D., Storch-Bergmann T., González Delgado R. M., Cid Fernandes R., Heckman T., Leitherer C., Schmitt H. R., 2003, *MNRAS*, 339, 772
- Reunanen J., Kotilainen J. K., Prieto M. A., 2002, *MNRAS*, 331, 154.
- Riffel R. A., 2010a, *Ap&SS*, 327, 239
- Riffel R. A., Storch-Bergmann T., Winge C., Barbosa F. K. B., 2006, *MNRAS*, 373, 2
- Riffel R., Rodríguez-Ardila A., Pastoriza M. G., 2006, *A&A*, 457, 61
- Riffel R., Pastoriza M. G., Rodríguez-Ardila A., Maraston C., 2007, *ApJL*, 659, 103
- Riffel R. A., Storch-Bergmann T., Winge C., McGregor P. J., Beck T., Schmitt H., 2008, *MNRAS*, 385, 1129
- Riffel R., Pastoriza M. G., Rodríguez-Ardila A., Maraston C., 2008, *MNRAS*, 388, 803
- Riffel R., Pastoriza M. G., Rodríguez-Ardila A., Bonatto C., 2009, *MNRAS*, 400, 273
- Riffel R. A., Storch-Bergmann T., Dors O. L., Winge C., 2009a, *MNRAS*, 393, 783
- Riffel R. A., Storch-Bergmann T., McGregor P. J., 2009b, *ApJ*, 698, 1767
- Riffel R. A., Storch-Bergmann T., Riffel R., Pastoriza M. G., 2010b, *ApJ*, 713, 469

- Riffel R., Riffel R. A., Ferrari F., Storchi-Bergmann T., 2011, *MNRAS*, 416, 493
- Riffel R., Rodríguez-Ardila A., Aleman I., Brotherton M. S., Pastoriza M. G., Bonatto C., Dors O. L., 2013, *MNRAS*, 430, 2002
- Riffel R. et al., 2015, *MNRAS*, 450, 3069
- Riffel R. A. et al., 2015a, *MNRAS*, 446, 2823
- Riffel R. A., Storchi-Bergmann T., Riffel R., 2015b, *MNRAS*, 451, 3587
- Riffel R. A. et al., 2016, *MNRAS*, 461, 4192
- Riffel R. A., Storchi-Bergmann T., Riffel R., Dahmer-Hahn L. G., Diniz M. R., Schönell A. J., Dametto N. Z., 2017, *MNRAS*, 470, 992
- Riffel R. A. et al., 2018, *MNRAS*, 474, 1373
- Rodríguez-Ardila A., Mazzalay X., 2006, *MNRAS*, 367, 57
- Rodríguez-Ardila A., Viegas S. M., 2003, *MNRAS*, 340, 33
- Rodríguez-Ardila A., Pastoriza M. G., Viegas S. M., Sigut T. A. A., Pradhan A. K., 2004, *A&A*, 425, 457
- Rodríguez-Ardila A., Contini M., Viegas S. M., 2005a, *MNRAS*, 357, 220
- Rodríguez-Ardila A., Riffel R., Pastoriza M. G., 2005b, *MNRAS*, 364, 1041
- Rosario D. J., Whittle M., Nelson C. H., Wilson A. S., 2010, *MNRAS*, 408, 565
- Rosario D. J., Togi A., Burtscher L., Davies R., Shimizu T., Lutz D., 2019, *ApJ*, 875, 8
- Schartmann M., Burkert A., Krause M., Camenzind M., Meisenheimer K., Davies R. I., 2010, *MNRAS*, 403, 1801
- Schartmann M., Wada K., Prieto M. A., Burkert A., Tristram K. R. W., 2014, *MNRAS*, 445, 3878
- Schnorr-Müller A., Storchi-Bergmann T., Nagar N. M., Robinson A. Lena D., Riffel R. A., Couto G. S., 2014, *MNRAS*, 437, 1708
- Schönell, Jr. A. J., Storchi-Bergmann T., Riffel R. A., Riffel R., 2017, *MNRAS*, 464, 1771
- Sersic J. L., Pastoriza M., 1967, *PASP*, 79, 152
- Simpson C., Forbes D. A., Baker A. C., Ward M. J., 1996, *MNRAS*, 283, 777
- Somerville R. S., Hopkins P. F., Cox T. J., Robertson B. E., Hernquist L., 2008, *MNRAS*, 391, 481
- Storchi-Bergmann T., Schnorr-Müller A., 2019, *NatAs*, 3, 48.
- Storchi-Bergmann T., Winge C., Ward M. J., Wilson A. S., 1999, *MNRAS*, 304, 35
- Storchi-Bergmann T., McGregor P., Riffel R. A., Simões Lopes R., Beck T., Dopita M., 2009, *MNRAS*, 394, 1148
- Storchi-Bergmann T., Simões Lopes R., McGregor P., Riffel R. A., Beck T., Martini P., 2010, *MNRAS*, 402, 819
- Storchi-Bergmann T., Riffel R. A., Riffel R., Diniz M. R., Borges Vale T., McGregor P. J., 2012, *ApJ*, 755, 87
- Ulvestad J. S., Wilson A. S., 1984, *ApJ*, 285, 439
- Veilleux S., Cecil G., Bland-Hawthorn J., 2005, *ARA&A*, 43, 769
- Zibetti S., Gallazzi A., Charlot S., Pierini D., Pasquali A., 2013, *MNRAS*, 428, 1479

This paper has been typeset from a $\text{\TeX}/\text{\LaTeX}$ file prepared by the author.